

## Variability of volume transport in the Taiwan Strait and its response to tropical MJO convection: A numerical approach

Haowei Sun <sup>a,b,d</sup>, Zhaoyun Chen <sup>c</sup>, Zhonghua Zhao <sup>a,b</sup>, Mengdi Xu <sup>a,b</sup>, Yimin Zhang <sup>a,b</sup>,  
Xiao-Hai Yan <sup>d</sup>, Xueding Li <sup>e,\*</sup>, Yuwu Jiang <sup>a,b,f,\*\*</sup>

<sup>a</sup> State Key Laboratory of Marine Environmental Science, Xiamen University, Xiamen, 361102, PR China

<sup>b</sup> College of Ocean and Earth Sciences, Xiamen University, Xiamen, 361102, PR China

<sup>c</sup> Guangdong Provincial Key Laboratory of Marine Disaster Prediction and Prevention, Institute of Marine Sciences, Shantou University, Shantou, 515063, PR China

<sup>d</sup> College of Earth, Ocean and Environment, University of Delaware, Newark, DE 19716, USA

<sup>e</sup> Fujian Marine Forecasts, Fuzhou, Fujian Province, 35001, PR China

<sup>f</sup> National Observation and Research Station for the Taiwan Strait Marine Ecosystem, Xiamen University, Xiamen, 361102, PR China

### ARTICLE INFO

#### Keywords:

Taiwan Strait  
Volume transport  
Numerical model  
Along-strait wind stress  
MJO convection  
Wave train

### ABSTRACT

Taiwan Strait (TWS) plays a crucial role in material exchange and nutrient budget between the South China Sea and the East China Sea. In this study, we investigate the variability of volume transport in the TWS and its response to tropical Madden–Julian Oscillation (MJO) convection based on the simulated results from a three-dimensional operational numerical model. Validated by the observational data, the model generally reproduced the physical field well. The volume transport in the TWS has strong seasonal cycles as well as higher-frequency variations. Intra-seasonal fluctuations dominate the along-strait currents variability, while secondary and the last signal are seasonal one and inter-annual variability, respectively. Overall, the along-strait wind stress plays a more important role in controlling the variability of volume transport in the TWS than the pressure gradient induced by north-to-south sea level slope. At intra-seasonal time scales, the volume transport in the TWS varies with the movement of the tropical MJO convection from Indian Ocean eastward to the western Pacific Ocean. These oceanic anomalies are related to atmospheric anomalies, with a distinct physical linkage from the tropical atmosphere to the mid-latitude ocean. The tropical MJO deep convection can modify the upper tropospheric heights and generate a wave train pattern that propagates to mid-latitudes. In addition, these anomalous upper tropospheric heights modulate the surface pressure, resulting in a cyclonic anomaly. The upper tropospheric heights anomaly and its corresponding mean sea level pressure anomaly move eastward in the MJO cycle following the migrating MJO heat source in the tropics from phase 2 to 5. Consequently, surface winds change as the cyclonic anomaly moves from central China to the east of Japan, resulting in a northeast volume transport anomaly during MJO phase 2 and 3 and a southwest volume transport anomaly during MJO phase 4 and 5.

### 1. Introduction

The Taiwan Strait (TWS) is a 350-km-long and 180-km-wide water channel connecting the South China Sea (SCS) and East China Sea (ECS). Although its bathymetry is very shallow in most parts, the TWS includes topographic features that can influence its circulation pattern remarkably. The Taiwan Bank, with a depth of less than 20 m, is an underwater shoal in the southern part of the TWS. On its east side,

the canyon Penghu Channel (PHC) connects the Wuqiu Depression in the northwest, forming an important pathway through which water from the south intrudes into the TWS. The Zhangyun Ridge, with a depth of less than 20 m, is located to the north of the PHC (Fig. 1b). Affected by East Asia monsoon system, the southwest summer monsoon is dominant in the TWS from June to August, with an average wind speed of 5.1 m/s, whereas the northeast monsoon during the other seasons is much stronger, with an average wind speed of 10.2 m/s (Hu et al., 2010).

**Abbreviations:** CC, correlation coefficients; ECS, East China Sea; MJO, Madden–Julian Oscillation; OLR, Outgoing long wave radiation; RMSE, root-mean-squared errors; ROMS, Regional Ocean Modeling System; SCS, South China Sea; SPRC, Standard partial regression coefficients; SVD, Singular value decomposition; TWS, Taiwan Strait

\* Corresponding author.

\*\* Corresponding author at: State Key Laboratory of Marine Environmental Science, Xiamen University, Xiamen, 361102, PR China.

**E-mail addresses:** [hwsun@udel.edu](mailto:hwsun@udel.edu) (H. Sun), [chenzy@stu.edu.cn](mailto:chenzy@stu.edu.cn) (Z. Chen), [zhaozh@stu.xmu.edu.cn](mailto:zhaozh@stu.xmu.edu.cn) (Z. Zhao), [md.xu@outlook.com](mailto:md.xu@outlook.com) (M. Xu), [Haikhezhangyimin@163.com](mailto:Haikhezhangyimin@163.com) (Y. Zhang), [xiaohai@udel.edu](mailto:xiaohai@udel.edu) (X.-H. Yan), [lxd007@xmu.edu.cn](mailto:lxd007@xmu.edu.cn) (X. Li), [ywjiang@xmu.edu.cn](mailto:ywjiang@xmu.edu.cn) (Y. Jiang).

<https://doi.org/10.1016/j.ocemod.2023.102240>

Received 12 January 2023; Received in revised form 12 July 2023; Accepted 12 July 2023

Available online 17 July 2023

1463-5003/© 2023 Elsevier Ltd. All rights reserved.

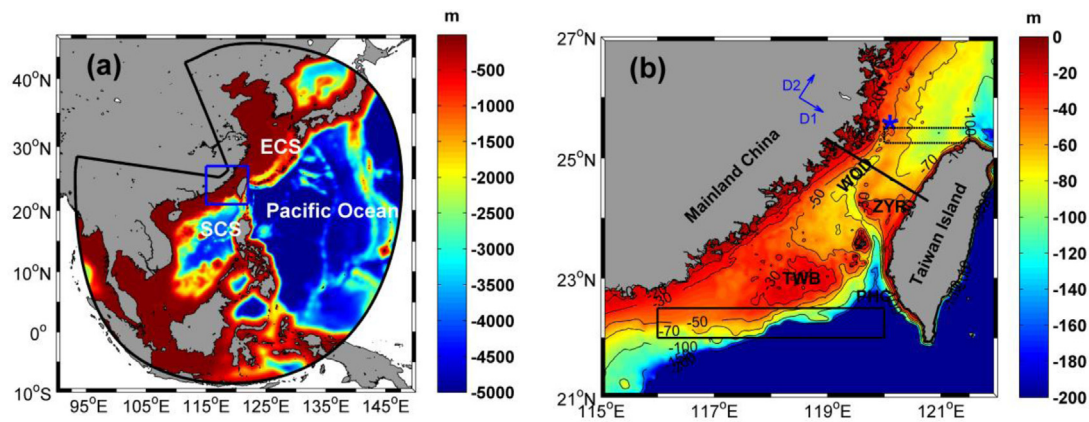


**Fig. 1.** (a) The model domain of Taiwan Strait Nowcast\Forecast system (TFOR) and (b) the bottom topography of the TWS. (a) The black line refers to the TFOR's domain, while the blue box shows the location of the TWS that is zoomed-in in (b). ECS and SCS denote East China Sea and South China Sea, respectively. (b) TWB, ZYR, and WQD denote Taiwan Bank, Zhangyun Ridge, and Wuqiu Depression, respectively. The blue star indicates the location of the buoy for current validation. D1 and D2 are the cross-strait and along-strait directions, respectively. The black line denotes the section used for volume transport analysis. The solid and dashed black boxes indicate the locations where the sea level of the southern strait and northern strait are averaged, respectively.

Owing to the essential role in material exchange and nutrient budget between the SCS and the ECS, volume transport through the TWS has been studied for decades using both observational data (e.g., Wyrтки, 1961; Fu et al., 1991; Wang et al., 2003; Lin et al., 2005; Jan et al., 2006) and numerical models (e.g., Wu and Hsin, 2005; Zhang et al., 2009, 2013, 2014). Wyrтки (1961) proposed that the transport in the TWS is northward in summer and southward in winter based on sea level data obtained from both sides of the TWS. Similarly, Fu et al. (1991) came up with a net northward transport all year round using limited measured current data taken from hydrographic cruises. They reported its magnitude to be 3.32 Sv in summer and  $-1.74$  Sv in winter ( $1 \text{ Sv} = 10^6 \text{ m}^3/\text{s}$ ; positive value represents northeastward transport, while negative value is for southwestward transport). Wang et al. (2003) derived a mean transport of 1.8 Sv in the TWS that might range from 2.7 Sv in summer to 0.9 Sv in winter by analyzing a 2-year ship-board acoustic Doppler profiler data. In comparison, Lin et al. (2005) showed a much weaker mean transport of  $0.12 \pm 0.33$  Sv during winter, with its instantaneous value varying from  $-5$  Sv to 2 Sv. They reported their findings based on the data from four bottom-mounted Acoustic Doppler Current Profilers (bm-ADCP) deployed across the TWS from September 28 to December 14 of 1999 when the northeast monsoon was intense. Similar results could be found in the numerical study performed by Wu and Hsin (2005), which derived an annual average transport of 1.09 Sv. They also showed that the sea water flux was northward and the largest in summer but minimum and even southward in fall and winter. Zhang et al. (2014) obtained an annual mean transport of 0.78 Sv through the TWS by using a shallow water model forced by high spatio-temporal resolution meteorological data. Their simulation results also suggested a southward transport in December and a northward transport in June.

The volume transport through the strait is usually subject to wind stress (Wyrтки, 1961; Guo et al., 2005; Jan et al., 2006), sea level slope (Guo et al., 2005; Yang, 2007; Li et al., 2018), oceanic eddies (Chang et al., 2015), synoptic events (Ko et al., 2003; Zhang et al., 2009, 2013, 2014), etc. In the TWS, a northward flow persists in all seasons despite that the annual mean wind stress is strongly southward. Since both wind stress and friction act against the northward flow during winter, the transport frequently against the wind is due to the north-to-south sea level slope induced by open-ocean forcing (e.g., Kuroshio path) (Chuang, 1985, 1986; Yang, 2007). However, the East Asia monsoon system is regarded as the main factor contributing to the seasonal variability of the transport in the TWS (Guo et al., 2005; Jan et al., 2006). A simple linear regression equation between wind stress and volume transport through the TWS was provided by Wu and Hsin (2005), and the result showed that the correlation

coefficient was as high as 0.82. Generally, the along-strait current in the TWS is influenced by the combined effect from two forces: East Asia monsoon and the southward pressure gradient induced by sea level slope. In summer, these two forces are in the same direction, resulting in a stronger volume transport in the TWS. The competition between northeast monsoon and the background southward pressure gradient during winter leads to a weak northward or even reversed flow. In addition, transport in the TWS could also be affected by short-term synoptic events such as coastally trapped waves generated by northerly winter wind bursts (Ko et al., 2003) and typhoons (Zhang et al., 2009, 2013, 2014). A numerical study presented by Zhang et al. (2014) showed that typhoons had an accumulative influence, which reduced not only the monthly mean transport by up to 0.45 Sv but also the annual mean transport by 0.09 Sv (more than 10% of the annual mean transport in the TWS). Moreover, mesoscale eddies can alter the transport in the TWS as well. In the idealized experiments, Chang et al. (2015) pointed out that eddies can affect the intra-seasonal variability of the current in the TWS by creating external forcing. In particular, the warm eddy southwest of Taiwan tended to generate a northward transport, while the cold eddy led to a southward flow.

As a well known atmospheric phenomenon in the equatorial region, Madden-Julian Oscillation (MJO) is a major mode of atmospheric fluctuation on weekly to monthly timescales (Madden and Julian, 1971, 1972). According to Wheeler and Hendon (2004), MJO events can be determined by using multivariate empirical orthogonal function analysis of 200-hPa zonal winds, 850-hPa zonal winds, and satellite-based outgoing long wave radiation (OLR) data in the near-equatorial region. The MJO events are categorized into eight different phases, i.e., Phases 1 to 8 based on the two leading principal component time series [the Real-time Multivariate MJO series 1 (RMM1) and 2 (RMM2)] in a two-dimensional phase space. Generally, active MJO events appear as atmospheric deep convection propagating eastward from western Indian Ocean to the Maritime Continent; tracing anticlockwise circles around the origin in the phase space [see Fig. 7 in Wheeler and Hendon (2004)]. The direct influences of MJO on the tropical ocean have been well documented in the literatures (Jones et al., 1998; Kashino et al., 1999; Shinoda et al., 2013; Waliser, 2003). The indirect impacts of MJO on the subtropical ocean, however, have drawn little attention. Among these studies, Isoguchi and Kawamura (2006) revealed that the intensification of southwesterly monsoon and resultant sea surface temperature cooling occur with the MJO in the SCS in summer. Based on the simulated results from three types of numerical models, Wang et al. (2013) demonstrated that the MJO enhanced both positive wind stress curl over the northern SCS and negative wind stress curl over the southern SCS. They also showed

that the MJO induced a stronger cyclonic gyre in the northern SCS and anticyclonic gyre in the southern SCS during its westerly phase, while the reverse effect was observed in its easterly phase. Barrett et al. (2017) noted a wind-driven response of the surface current anomalies along the U.S. west coast related to MJO. Nonetheless, the impacts of MJO on the circulation pattern and volume transport in the TWS have rarely been explored.

In this study, volume transport through the TWS was simulated and investigated by using a three-dimensional operational ocean model validated by observational data. The remaining of this paper is organized as follows. Section 2 briefly introduces the numerical model used in this study and its validation with observational data. In Section 3, we describe the mean state and the variability of volume transport in the TWS. We also apply a multivariable linear regression equation to the model results to evaluate the relative importance of sea level slope and wind stress in transport variability through the TWS. In Section 4, we examine the indirect impact of tropical MJO convection on the current pattern and volume transport in the TWS. In the last section, the results are summarized, and the conclusions are drawn.

## 2. Numerical model and methods

### 2.1. Model configuration and validation

The numerical model employed in this study is based on the Regional Ocean Modeling System (ROMS). ROMS is a free-surface, hydrostatic ocean model that solves Reynolds-averaged Navier–Stokes equations on topography-following coordinates (Shchepetkin and McWilliams, 2003, 2005). The model is derived from the operational TWS Nowcast/Forecast system (TFOR), which is capable of not only simulating multi-scale process in the ocean, but also providing various ocean forecasts. The performance of TFOR has been assessed and validated extensively, while its results have been widely used in studying various oceanic processes in the TWS (Wang et al., 2016; Chen et al., 2014; Lin et al., 2016; Liao et al., 2013, 2018; Zhao et al., 2020).

The orthogonal curvilinear grid (Fig. 1a) covers the northwestern Pacific Ocean, extending from 8.5°S to 45°N and 93° to 148°E, and its horizontal resolution ranges from 1.5 km in the TWS to 45 km near the open boundary. The model bathymetry is derived from the combination of digitized survey data published by the China Maritime Safety Administration and ETOPO2v2 from the National Geophysical Data. A weak depth filter has been applied to smooth the bathymetry so as to reduce any unexpected diapycnal mixing error. A total of 30 vertical topography-following layers with higher resolution layers near the surface were adopted.

The 6-hourly air–sea flux data, consisting of momentum flux, heat flux, and freshwater flux, were interpolated from ERA5 produced by European Centre for Medium-Range Weather 40 Forecasts (ECMWF, <https://cds.climate.copernicus.eu/cdsapp#!/dataset/reanalysis-era5-single-levels?tab=form>) and provided to the model as surface forcing following bulk formulation scheme (Liu et al., 1979). The Estimating the Circulation and Climate of the Ocean, PhaseII (ECCO2) data set ([http://apdrc.soest.hawaii.edu/datadoc/ecco2\\_cube92.php](http://apdrc.soest.hawaii.edu/datadoc/ecco2_cube92.php)), comprising sea level, velocity, temperature, and salinity, was used to extract lateral open boundary conditions. The monthly mean river discharges along the mainland coast, including data from the Yangtze River, Pearl River, Yalu River, Liaohe River, Luanhe River, Ou River, Minjiang River, Jiulong River, and Hanjiang River, are also considered in this model, with their salinities set at zero.

The fourth-order centered difference was set as the scheme for both two-dimensional and three-dimensional advection terms in the momentum and tracer equations. The Smagorinsky-like diffusion was used for harmonic horizontal mixing along the geopotential surface in the tracer equations, while the harmonic horizontal mixing of momentum occurred along constant sigma surfaces. The vertical turbulent

**Table 1**

Comparison metrics between the modeled and observed velocity components (both along-strait and cross-strait directions involved) in the surface, middle, and bottom layers, as well as the vertical mean velocity components at the station of the bottom-mounted ADCP (Fig. 1b).

	CC	RMSE (m s <sup>-1</sup> )	CC	RMSE (m s <sup>-1</sup> )
6 m	0.76	0.28	0.33	0.13
26 m	0.79	0.20	0.09	0.09
46 m	0.74	0.13	0.54	0.08
Mean	0.82	0.17	0.33	0.06
	Along-strait		Cross-strait	

CC: Correlation coefficients; RMSE: Root-mean-squared errors.

mixing parameterization scheme of momentum and tracers was carried out using the Mellor and Yamada (1982) (MY2.5) turbulence module. Chapman boundary conditions (Chapman, 1985) and Flather boundary conditions (Flather, 1987) were employed for surface elevation and two-dimensional momentum, respectively. Clamped boundary conditions were applied for three-dimensional momentum and tracers.

The model was spun up from the initial condition derived from ECCO2 data on January 1, 2010. The simulated results from January 1, 2011, to December 31, 2020 were used in this study. To evaluate the performance of TFOR, Fig. 2 shows the modeling velocities at depths of 6 m, 26 m, and 46 m from July 1, 2014, to March 19, 2015, with one buoy data deployed near the coast region of the strait (the location is shown in Fig. 1b) during the same time period for comparison. The  $x$  and  $y$  directions are rotated 32° clockwise, with positive  $x$  pointing cross-strait southeastward and positive  $y$  pointing along-strait northeastward (the rotated coordinate is shown in Fig. 1b). Meanwhile, the tidal and inertial signals are excluded by applying the 36-hour low-pass-filter to the buoy and modeling data. The along-strait currents in the observed data displayed similar temporal variations over the entire water column (Fig. 2a–2d), indicating a vertical uniformity in the along-strait direction, whereas the cross-strait currents did not show such vertical coherence. The mean and standard deviation for the observed vertically mean velocity were  $-0.07$  m s<sup>-1</sup> and  $0.29$  m s<sup>-1</sup>, respectively (Fig. 2d), while those in the cross-strait direction, in comparison, were  $0.03$  m s<sup>-1</sup> and  $0.04$  m s<sup>-1</sup>, respectively (Fig. 2h), suggesting that the current variation mainly occur in the along-strait direction. The along-strait currents generally flowed northward from July 1 to August 31 and southward during the rest period of time, especially in the surface and middle layers.

The model generally reproduced the same temporal variations in the observational data. For example, the northward current dominated almost all the observing period, except in the upper layer where the flow was frequently affected by China coastal current in winter. Table 1 provides the comparison metrics between the model outputs and the buoy data. The correlation coefficients (CC) and root-mean-squared errors (RMSE) for vertically mean along-strait velocity between the model outputs and the buoy data were 0.82 and  $0.17$  m s<sup>-1</sup>, respectively. In comparison, these values for vertically mean cross-strait velocity were 0.33 and  $0.06$  m s<sup>-1</sup>, respectively. In general, the model captured basic spatial and temporal tendency as the buoy data. In addition, the velocity reproduction was better in the along-strait direction than that in the cross-strait direction. Fig. 2 also revealed that the buoy data had a slightly broader velocity range at surface than the model outputs in both the along-strait and cross-strait directions, which might be attributed to the relatively smaller wind speed of ERA data in the TWS compared to the observations (Kuang et al., 2015).

### 2.2. Singular value decomposition (SVD) analyses

SVD is a matrix factorization technique commonly used in linear algebra and numerical analysis. It determines the correlation between two fields, with each mode explaining a fraction of the covariance. One of the advantages of SVD analysis is that the spatial component of the

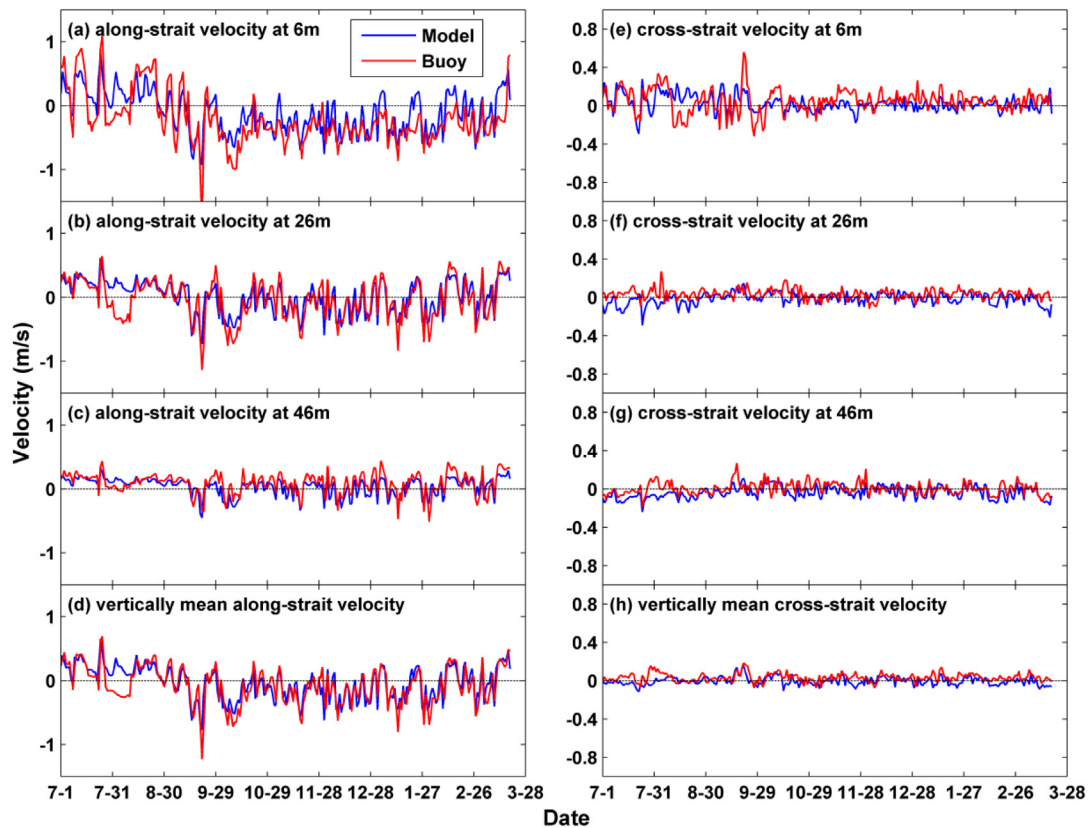


Fig. 2. Current verification in the (a–d) along-strait and (e–h) cross-strait directions at 6 m, 26 m, and 46 m, in addition to its vertical mean. The blue lines indicate the current velocity from model outputs, while the red lines indicate the current velocity from buoy observations. The location of the buoy is shown as the blue star in Fig. 1b.

two variables can vary in dimension, although the time dimension of the two fields must be equal. SVD has various applications in fields such as data analysis, signal processing, image compression, and machine learning.

The use of SVD in this study is briefly described below. First, the standardized daily along-strait wind stress anomalies in the TWS (an  $m \times t$  matrix) and standardized daily along-strait velocities in the section (an  $n \times t$  matrix) were developed and SVD was applied to the cross-covariance matrix between these two fields. Consider  $A$  is an  $m \times n$  cross-covariance matrix developed by multiplying along-strait wind stress matrix with the transpose of along-strait velocities matrix and divided by the number of days, the SVD factorizes it into the product of three matrices as follows:

$$A = U \Sigma V^T \quad (1)$$

Here,  $U$  is an  $m \times m$  unitary matrix, meaning its columns are orthogonal to each other and have a magnitude of 1. The columns of  $U$  are known as the left singular vectors of  $A$ .  $\Sigma$  is an  $m \times n$  diagonal matrix with non-negative real numbers on the diagonal, arranged in descending order. These diagonal elements are known as the singular values of  $A$ .  $V^T$  is the transpose of an  $n \times n$  unitary matrix  $V$ . Like  $U$ , the columns of  $V$  are orthogonal to each other and have a magnitude of 1. The columns of  $V$  are known as the right singular vectors of  $A$ . Each pair of singular vectors explains a fraction of the covariance between the two fields. The singular values in  $\Sigma$  represent the importance of the corresponding singular vectors pairs, with the first pair explaining the largest fraction.

To measure the relative importance of each mode in the decomposition, the squared covariance fraction (SCF) is then calculated. Each singular value in  $\Sigma$  is squared and divided by the sum of all the squared singular values to yield a percentage of squared covariance for each mode. To describe how the spatial patterns evolve in time, each of the corresponding pair of singular vectors is projected onto

its own original data field, yielding the temporal expansion series. For instance, the left (right) temporal expansion series was obtained by projecting the left (right) singular vector onto the original along-strait wind stress (along-strait velocities) matrix. Finally, the left (right) heterogeneous correlation map (for the first mode) was developed by correlating the right (left) temporal expansion series with along-strait wind stress (along-strait velocities) matrix. In this study, right heterogeneous correlation map of the first mode was produced to study the relative importance of the along-strait wind stress on the volume distribution through the TWS.

### 3. Analysis of volume transport through the TWS

#### 3.1. Mean state and variability of volume transport through the TWS

The 10-year (2011–2020) mean along-strait current distribution in the profile (the location is shown in Fig. 1b) and its standard deviation are plotted in Fig. 3, along with the monthly climatology of the volume transport in the TWS. The climatological volume transport in the TWS shows a strong seasonal cycle, with a maximum of 2.79 Sv in July and a minimum of  $-0.12$  Sv in December (Fig. 3c). The annual mean transport was 1.23 Sv, while the winter (December–February), spring (March–May), summer (June–August), and autumn (September–November) transport were 0.13 Sv, 1.79 Sv, 2.57 Sv, and 0.42 Sv, respectively. These estimates are consistent with the published observations based on the bm-ADCP measurements (Lin et al., 2005; Jan et al., 2006). The corresponding standard deviations in monthly transport indicate that a larger transport variability was observed in winter than in summer. This is likely due to the more energetic wind fluctuations in winter than in summer (e.g., the standard deviation of the along-strait wind stress was  $0.08 \text{ N m}^{-2}$  in summer but  $0.16 \text{ N m}^{-2}$  in winter, figure not shown). As shown in Fig. 3a, the mean along-strait current structure denotes two major sources contributing the most to the northward

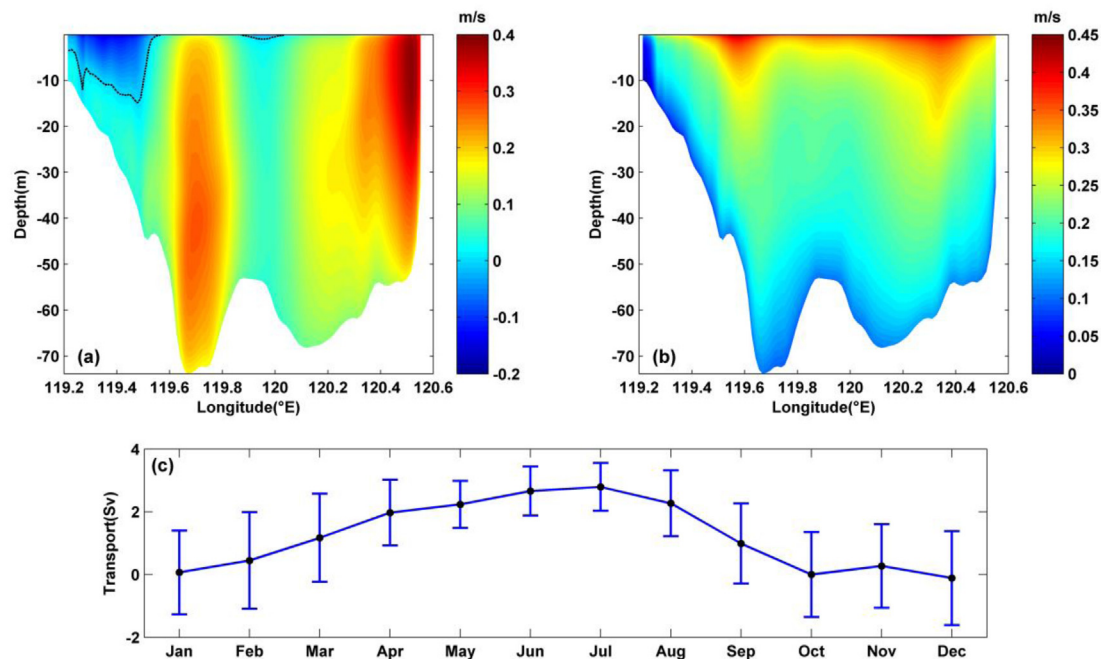


Fig. 3. (a) Mean and (b) standard deviation of the along-strait current distribution in the profile. (c) Monthly mean volume transport (blue curve with black dots) in the TWS and its corresponding error bars (two standard deviations). Mean and standard deviation are derived from the model output in the period between January 2011 and December 2020. The section for transport calculation is shown in Fig. 1b. The dashed curves in (a) denote zero contours.

transport in the TWS. One of them is the Wuqiu Depression, which is a deep trough through which warm and salty water from the south flow into the TWS, while the other source is located near the western coast of Taiwan where the mean along-strait current speed reaches up to  $40 \text{ cm s}^{-1}$ . This is because bathymetry affects the northward intrusion from PHC to separate into two branches (Jan et al., 2002). On the other hand, the southward flow above the zero contours along the western coast of the strait represents the influence of China coastal current whose width scales well with the internal deformation radius (roughly 30 km in the TWS). This current is assumed to be buoyancy-driven (Wu et al., 2013), which usually brings in cold, fresh, and nutrient-rich water from several river plumes along Chinese coast southward during winter. The surface currents in the TWS are significantly affected by wind stress, which not only reverse seasonally but also fluctuates at synoptic time scale, and results in higher standard deviation of along-strait current at the surface (Fig. 3b). In addition, the variability of the current becomes weak near the bottom region, where the flows are constantly influenced by south-to-north pressure gradients (Yang, 2007).

Fig. 4a presents original simulated daily transport from 2011 to 2020. The transport ranged from  $-4.8$  to  $4.6 \text{ Sv}$  with its standard deviation of  $1.6 \text{ Sv}$ , indicating strong seasonal cycles as well as higher-frequency variations. Also shown is the time series after removing intra-seasonal variations and higher-frequency signals at the synoptic time scales utilizing a 200-day low-passed filter (red curve in Fig. 4a). This time series illustrated that the transport is strong and northward in summer, but weak or even southward in winter. At the inter-annual time scales, the volume transport also exhibited year-to-year difference. Our findings showed that the transport was strong in 2017 and 2020 (one standard deviation beyond the mean transport), with its annual mean being  $1.47 \text{ Sv}$  and  $1.4 \text{ Sv}$ , respectively. In comparison, the transport was weak in 2012 (one standard deviation below the mean transport), with its annual mean being  $0.89 \text{ Sv}$ .

Spectral analyses based on the Fast Fourier Transform were applied to the depth-averaged along-strait velocities along the section to further investigate the variability of volume transport through the TWS in different time periods. Following Hsin et al. (2013), the spectra were categorized into three groups: time periods longer than 500 days,

between 200 days and 500 days, and shorter than 200 days. These time periods represented inter-annual time scales, seasonal time scales, and intra-seasonal including synoptic time scales, respectively. As shown in Fig. 4b, the dominant variations were found on time scales of 1 year along the section. At the inter-annual time scale, however, the along-strait currents display some spatial distributions. The inter-annual variability of the along-strait currents is weak in the near Fujian coastal region where China coastal current predominate during winter, while it is strong in the central and eastern part of the strait, especially in Wuqiu Depression  $\sim 119.8^\circ\text{E}$  where the warm and saline water from the southern strait usually flow northward in the TWS. Integrating the spectra in the frequency domain yields the explained variances of 200-days high pass filtered, 200–500-days band pass filtered, and 500-days low pass filtered depth-averaged along-strait velocities as a function of longitude in Fig. 4c. The intra-seasonal time scales, accounting for over 50% of the total variance with a larger explained variance ( $>60\%$ ) in both sides of the strait and the Wuqiu Depression, dominate the along-strait currents variability. The secondary signal is the seasonal one, which explains about 30%–45% of the total variance and show relatively higher values in the front region ( $\sim 119.6^\circ\text{E}$ , usually formed during winter) and the central strait. In comparison, the inter-annual signal generally accounts for only a small part of explained variance, which is less than 5% all along the section, with relatively higher values located in Wuqiu Depression.

While the transport variability at its seasonal time scales shows secondary signal in the total explained variance, its cause has been attributed to the seasonal reversal of monsoon in this area. Spectral analysis and its corresponding explained variance above indicates that the variability of volume transport through the TWS has large energy at its intra-seasonal time scales, which might be related to the fluctuating wind caused by biweekly passage of cold fronts in winter and frequent occurrence of typhoons in summer. Generally, the direct driving force to the volume transport in the TWS comes from East Asia monsoon and the along-strait sea level slope related to the open ocean (e.g., Kuroshio), although they vary at different time scales. Factors influencing the volume transport through the TWS will be investigated in the next section using SVD analysis and a multivariable linear regression model.

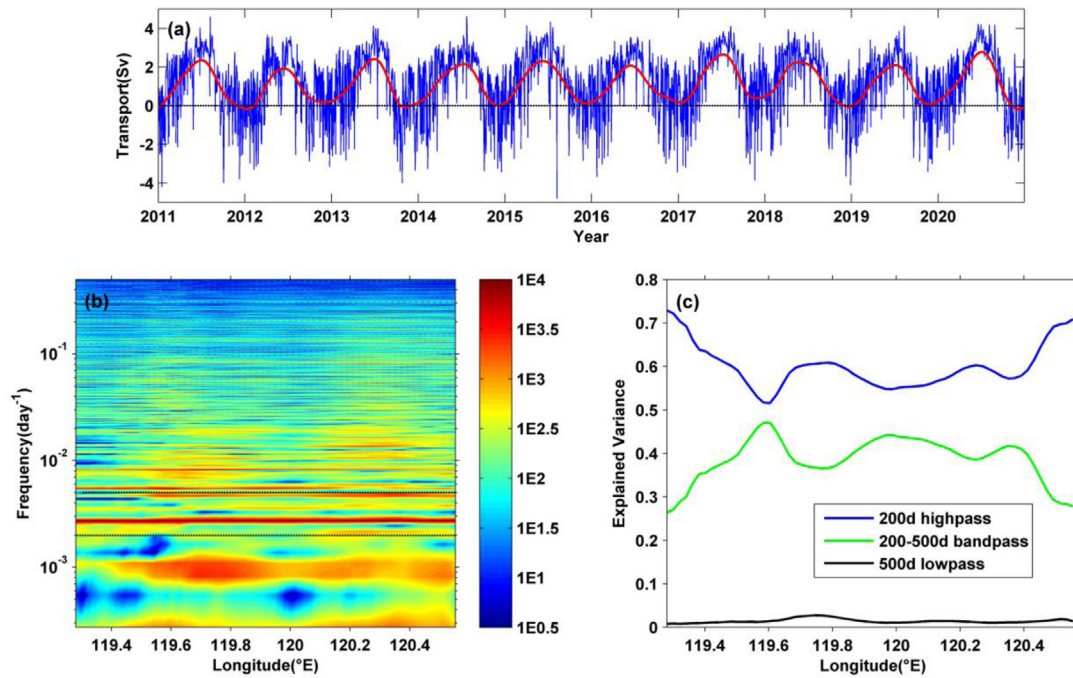


Fig. 4. (a) Time series of simulated transport (blue) through the TWS from 2011 to 2020 and its 200-day low-passed filtered results (red). The transport is derived from the section in Fig. 1b. (b) Longitude-dependent power spectra of normalized depth-averaged along-strait velocities. (c) Longitude-dependent explained variances of 200-days high pass (blue), 200–500-days band pass (green), and 500-days low pass (black) filtered depth-averaged along-strait velocities. Vertical dashed lines in (b) represent the periods of 200 days and 500 days.

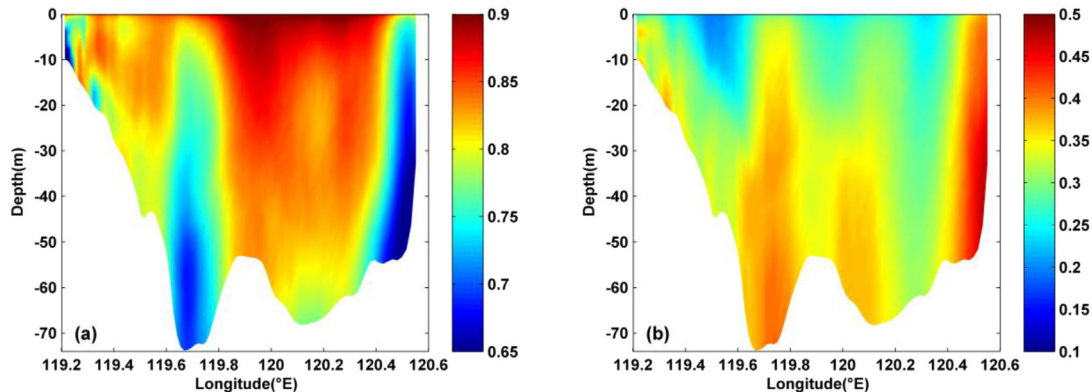


Fig. 5. (a) Heterogeneous correlation between along-strait current and first temporal expansion series of the wind stress. (b) Correlation coefficients distribution between along-strait current and sea level slope.

### 3.2. Effects of wind stress and sea level slope

To study the factors that influence volume transport through the TWS, we conducted a SVD analysis. This analysis was performed on the cross-covariance matrix between the wind field in the TWS and the along-strait current profile. The method used for this analysis is described in detail in Section 2.2. Accounting for 99% of the total variance, Fig. 5a displays right heterogeneous correlation map of the first mode, determined by correlating the along-strait current with first temporal expansion series of the wind stress. The CC were generally larger than 0.6, with higher values (>0.8) located near the central strait. In comparison, the correlation was relatively lower (<0.75) in Wuqiu Depression and in the near Taiwan Island. Fig. 5b shows the distribution of CC between along-strait current and sea level slope. The sea level slope was calculated by subtracting the mean sea level in the northern strait (120°–121.5°E, 25.25°–25.5°N, dashed black box in Fig. 1b) from the mean sea level in the southern strait (116°–120°E, 22°–22.5°N, solid black box in Fig. 1b). The results showed that the CC

range between 0.2 and 0.5, which are lower than most of the values in the heterogeneous correlation map. Interestingly, the CC between along-strait current and sea level slope show relatively higher value (>0.35) in the deep region of the Wuqiu Depression and in the near Taiwan Island, roughly matching the pattern displayed in the lower-CC area in the heterogeneous correlation map. These patterns indicate that while the monsoon serves as the primary force controlling the along-strait current; the south-to-north sea level slope related to open ocean also explains, in some degree, the variability of the along-strait current, especially in the deep region of the Wuqiu Depression and in the near Taiwan Island where the currents are frequently affected by warm and saline water from the southern strait (e.g., Kuroshio and South China Sea warm current).

Consider the linearized, shallow water momentum equations for a stable homogeneous fluid as follows:

$$-fv = -g \frac{\partial \eta}{\partial x} + \frac{\tau_{sx}}{H} - \frac{\tau_{bx}}{H} \quad (2)$$

$$fu = -g \frac{\partial \eta}{\partial y} + \frac{\tau_{sy}}{H} - \frac{\tau_{by}}{H} \quad (3)$$

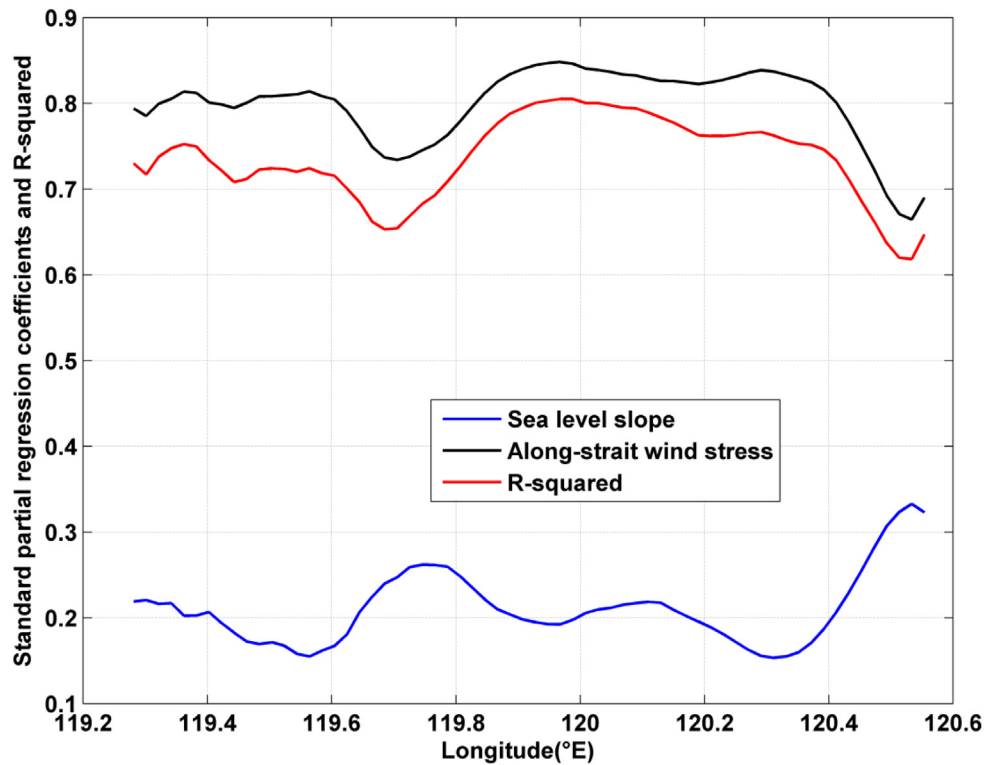


Fig. 6. Longitude-dependent of the standard partial regression coefficients for sea level slope (blue curve) and along-strait wind stress (black curve), along with the distribution of R-squared values (red curve) in the multivariable linear regression model.

Here,  $x$  and  $y$  are in the cross-strait and along-strait directions, respectively.  $H$  refers to the undisturbed water depth,  $\eta$  denotes surface elevation,  $\mathbf{u} = (u, v)$  denotes depth-averaged velocity, and  $f$  denotes the Coriolis parameter.  $\boldsymbol{\tau}_s = (\tau_{sx}, \tau_{sy})$  refers to kinematic wind stress, and  $\boldsymbol{\tau}_b = (\tau_{bx}, \tau_{by})$  refers to kinematic bottom stress, which can be parameterized as  $\boldsymbol{\tau}_b = \sigma H \mathbf{u}$ , where  $\sigma$  is a constant friction coefficient. Since the cross-strait velocity, wind stress, and bottom friction in the TWS are negligible in comparison to the along-strait components, Eq. (2) can be rewritten as

$$\sigma v = -g \frac{\partial \eta}{\partial y} + \frac{\tau_{sy}}{H} \quad (4)$$

This equation indicates that the along-strait current is driven by a balance between sea level slope and along-strait wind stress, although they vary at different time scales. In this study, the along-strait current was regressed against the sea level slope and the along-strait wind stress according to Eq. (3) by using the daily model outputs. In this multivariable linear regression model, the standard partial regression coefficients (SPRC) are calculated as a function of longitude to evaluate the relative importance of sea level slope and along-strait wind stress on the variability of the depth-averaged current in the TWS. As shown in Fig. 6, the goodness of the fit is between 0.61 and 0.81, suggesting a high correlation between the currents estimated using Eq. (3) and the model outputs. The SPRC for the along-strait wind stress (ranging from 0.65 to 0.85) is higher than that for sea level slope all along the section (ranging from 0.15 to 0.32). In addition, the SPRC for the along-strait wind stress showed relatively higher values in the Fujian coastal region and central strait, indicating the regions where wind dominates the current in the TWS. In contrast, the SPRC for the sea level difference displayed an inverse pattern, showing their relatively higher values in the Wuqiu Depression and the eastern TWS where the northeastward transport contributes the most. The goodness of the fit showed relatively lower values in Wuqiu Depression and the eastern TWS, following the trend of the SPRC for along-strait wind stress. This demonstrates that the along-strait wind stress is more important than

the pressure gradient in controlling the variability of volume transport in the TWS, which is in agreement with the result in the SVD analysis above.

In the frequency domain, the cross-spectral analysis in Fig. 7 also revealed that the along-strait wind stress and the volume transport through the TWS are significantly coherent, with the coherence generally larger than 0.6 at frequencies lower than 0.35 cycles per day (cpd). The sea level slope, in comparison, showed relatively lower coherence with the volume transport in the TWS at lower frequencies, although it became higher at frequencies higher than 0.12 cpd. The cross-strait sea level difference was obtained from both sides of the section (east minus west) and was found to be highly coherent with volume transport, as shown in Fig. 7. The coherence was larger than 0.9 through the frequency band. These values were far above the 99% confidence level of 0.23. The phase spectra indicate that both the along-strait wind stress and the sea level slope lead the volume transport in the TWS, while almost instantaneous response of the volume transport was observed to the variability of the cross-strait sea level difference. The along-strait wind stress led the transport for approximately 0–6 h in the frequency domain. These time lags are in agreement with the results reported by Shen et al. (2017), who suggested a significant coherence between the time coefficient of the first mode subtidal flows derived from empirical orthogonal function analysis and the alongshore wind, with the flows lagging wind by about 0–5.7 h. Chuang (1985) and Zhang et al. (2009) also suggested that a frictional adjustment time was required during which the along-strait wind stress accelerates or decays the flow. In the TWS, the Ekman layer depth and the turbulent friction coefficient are roughly 10 m and  $10^{-2} \text{ m}^2/\text{s}$ , respectively. This frictional adjustment time can be estimated as  $10^4 \text{ s}$ , and it modifies the cross-strait sea-level gradient via Ekman transport and induces an instantaneous response of the volume transport variability. In contrast, the volume transport takes a longer time, time lag of roughly 9–22 h, to respond to the sea level slope change. Liao et al. (2018) reported that the coastal-trapped waves took about 20 h to propagate toward the TWS from north. The time lag for the volume transport to respond to the sea level slope

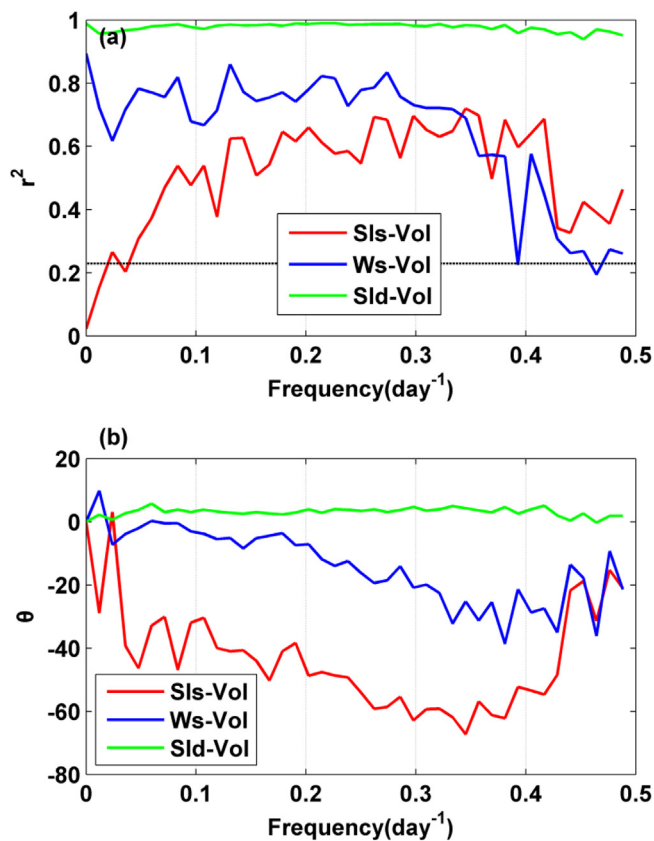


Fig. 7. (a) coherence squared and (b) phase between the volume transport through the TWS, the along-strait wind stress, the sea level slope, and the sea level difference cross the strait. Negative phases (blue line and red line) indicate that the volume transport lag the along-strait wind stress/ the sea level slope. The black dotted line in 7a represents the 99% significance level (0.23). Vol, Sls, Sld, and Ws in Figs. 7a and 7b denote volume transport through the TWS, the sea level slope, the sea level difference cross the strait and the along-strait wind stress, respectively.

change might be attributed to the time taken by coastal-trapped waves to propagate southward through the TWS. This modifies the changing cross-strait sea-level gradient and results in an instantaneous response of the volume transport variability.

#### 4. Response of winter-half year volume transport in the TWS to tropical MJO convection

As discussed in the above sections, the along-strait wind stress plays a more important role than pressure gradient in controlling the variability of volume transport in the TWS. In addition, the variability of volume transport through the TWS exhibits large energy at its intra-seasonal time scales. Previous studies have noted that MJO majorly impacts the winter (November–April) rainfall in Taiwan through anomalous anticyclones and increasing moisture supply in the subtropical atmospheric response (Hung et al., 2014). Thus, the anomalous tropical convection of the MJO is assumed to be physically linked with the volume transport through the TWS. This section investigates the response of volume transport of winter-half year in the TWS to tropical MJO convection.

##### 4.1. Winter-half year volume transport associated with MJO

The MJO can influence weather systems near TWS, leading to variations in wind patterns depending on the phase of the MJO. However, the specific wind conditions during MJO phases can vary based on local atmospheric conditions, interactions with other weather systems,

and the time of year. Generally, MJO phase 1 and 2 are often associated with enhanced convection in the Indian Ocean and can lead to increased wind speeds near TWS. During these phases, the prevailing winds are typically from the southeast or south, which can bring moist air and potentially stronger winds to the region. MJO phase 3 and 4 are more associated with enhanced convection over the western Pacific and the date line. While the convection is weaker near TWS, it can result in more stable atmospheric conditions. During these phases, the prevailing winds may become lighter and less consistent, often exhibiting variable or calm wind conditions in the TWS. MJO phase 5 and 6 are characterized by enhanced convection over the Indian Ocean and parts of the SCS. As the MJO progresses into these phases, TWS may experience increased easterly winds or northeasterly winds. These winds can be associated with the development or intensification of tropical cyclones in the region. MJO Phase 7 and 8 are usually associated with suppressed convection near TWS, resulting in drier conditions. During these phases, the prevailing winds may become weaker, with lighter easterly or northeasterly winds.

In the TWS, the East-Asia winter monsoon is much stronger compared to that during summer time. To exam the above mentioned MJO effects on the winter-half year volume transport through the TWS, the volume transport anomalies at the MJO time scales were pooled and averaged according to the different phases of the MJO. Here, the volume transport anomalies at the MJO time scales refer to the 20–100-day bandpass-filtered volume transport during November to April. In addition, a MJO index, which is calculated as the square root of sum squared RMM1 and RMM2, larger than 1 represents an active MJO event, whereas a MJO index less than 1 represents a weak MJO event. In this study, we did not include the daily volume transport with a weak MJO event. The winter-half year volume transport displayed northward anomaly in MJO phase 2 and southward anomaly in phase 5 (Fig. 8), with its anomalous magnitude being 0.14 Sv and  $-0.19$  Sv respectively, generally showing a decreasing trend in the MJO cycle. The volume transport anomalies mainly showed an increasing trend after MJO phase 5.

The current anomalies varied differently in the TWS from MJO phase 2 to 5 as the anomalous tropical MJO convection moved from Indian Ocean eastward to Maritime Continent. Fig. 9 shows the 20–100-day bandpass-filtered depth-averaged currents from MJO phase 2 through 5 and their corresponding wind stress anomalies. The entire strait displays strong northeastward movements in MJO phase 2, with large anomalies located on the west of the PHC. During MJO phase 3, the northeastward movements in the central strait gradually weaken. The current anomalies reverse to southwestward in the central strait in MJO phase 4, inducing a relatively weak negative transport anomaly. The magnitude of southwestward anomalies is the strongest in the entire strait during MJO phase 5, except for the region in the PHC where the northward flows are usually controlled by pressure gradient related to Kuroshio to the east Taiwan Island. The same composite of wind stress anomalies over the TWS show high correlation with current anomalies (Fig. 9(e)–(h)). The wind stress in the TWS showed strong northeastward anomalies in MJO phase 2 and weak northeastward anomalies in MJO phase 3. In contrast, it displayed weak southwestward anomalies in MJO phase 4 and strong southwestward anomalies in MJO phase 5. Since surface wind is highly correlated with air pressure systems, the geopotential heights of 200 hPa, sea level pressure, and its corresponding atmospheric circulations were further analyzed to determine the physical linkage between the anomalous tropical convection of the MJO and the winter-half year volume transport in the TWS.

##### 4.2. Mechanism of oceanic response to tropical MJO convection

The classic evolution and movement of the anomalous tropical convection of the MJO can be described by the phase composites of OLR anomaly at MJO time scale. Fig. 10 displays the 20–100-day bandpass-filtered OLR anomalies during November to April for each MJO phase.

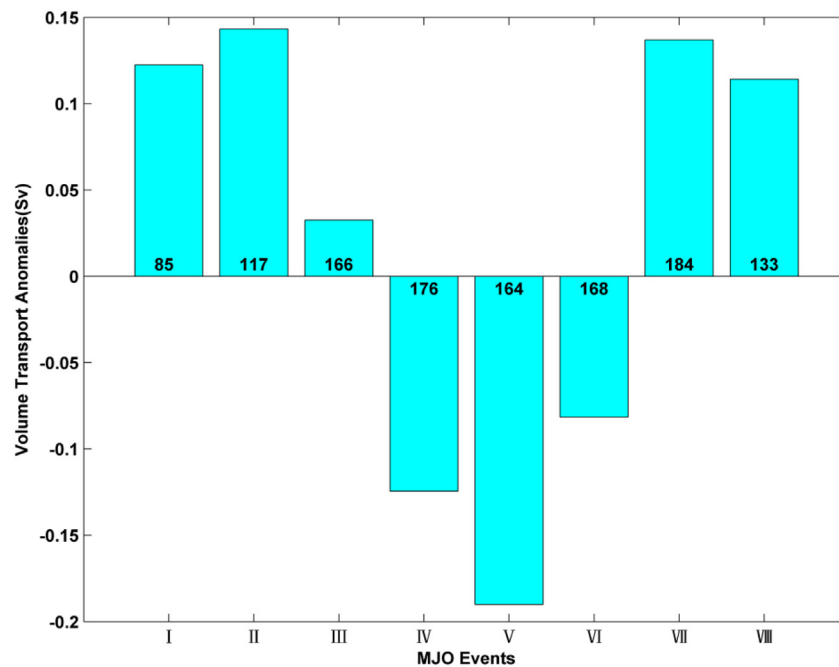


Fig. 8. The volume transport anomalies for MJO phases 1–8 in the winter half season (during November to April) from 2011 to 2020. The numbers at each bar denote the numbers of days for each MJO phase.

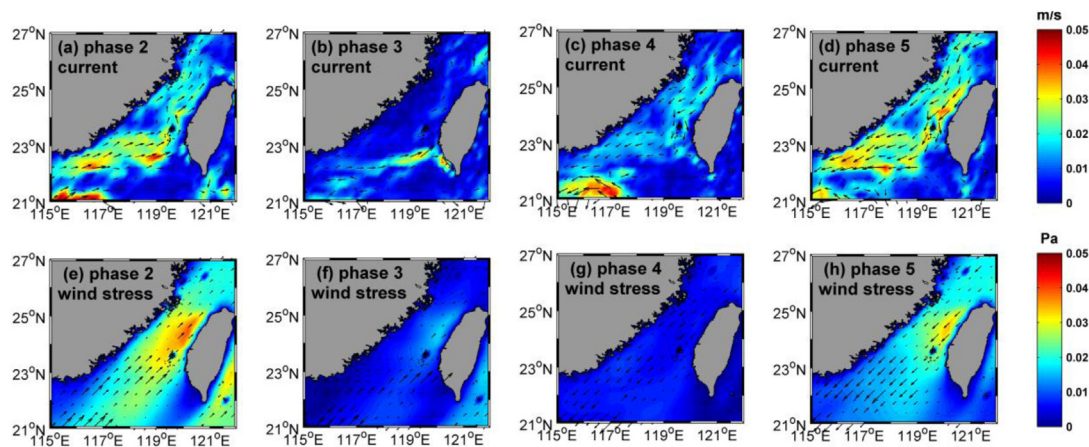


Fig. 9. Composite anomalous (a–d) depth-averaged current and (e–h) wind stress in the TWS for MJO phases 2–5. The color shading represents the magnitude of each field while the arrows denote their directions.

In MJO phase 1, the major deep convection of a growing event was observed over Africa and the western Indian Ocean. It then built in the Indian Ocean and moved eastward to the western Pacific Ocean as the time elapsed from phase 2 to 5. The deep convection continued to move eastward and finally dissipated near the International Date Line from MJO phase 6 to 8, while a shallower convection was generated and presented in the Indian Ocean.

The tropical atmospheric response to the MJO diabatic heating is a classic Matsuno–Gill-type pattern (Matsuno, 1966; Gill, 1980), which modulates the upper tropospheric heights and circulation via Rossby wave response and results in a pair of anomalous anticyclones symmetric about the equator to the west of the heating (Hsu, 1996). In the northern hemisphere, the anomalous anticyclone can further induce a wave train that propagates northeastward from tropical region to mid-latitude area. The wave train consists of a cyclonic anomaly and an anticyclonic anomaly in the mid-latitudes that influence several weather phenomena in the corresponding regions. This wave train moves with the movement of the MJO heat source eastward in the tropics.

Fig. 11 displays the composites of 200 hPa geopotential heights anomalies from MJO phase 2 to 5. During phase 3, the anomalous atmospheric 200 hPa geopotential heights showed a pair of anticyclone anomalies extending from 30°E to 80°E, with one centered at 25°N in the northern hemisphere and the other centered at 20°S in the southern hemisphere. In the northern hemisphere, the associated cyclonic anomaly is located at 30°N, extending from 90°E to 120°E, while the associated anticyclonic anomaly is centered at 45°N, extending from 130°E to 170°E. This planetary-scale atmospheric Rossby wave train response propagates eastward following the migrating MJO heat source as the MJO major deep convection moves from eastern Africa to the western Pacific Ocean. For example, the cyclonic anomaly in the wave train was centered in China in MJO phase 2. It migrated eastward and reached the east of Japan in MJO phase 5.

The above upper tropospheric heights anomalies and their corresponding circulation anomalies can project onto mean sea level pressure via quasi-geostrophic adjustment mechanisms (Carlson, 1991). Fig. 12 shows the composites of mean sea level pressure anomalies from MJO phase 2 to 5. Due to the corresponding wave train pattern

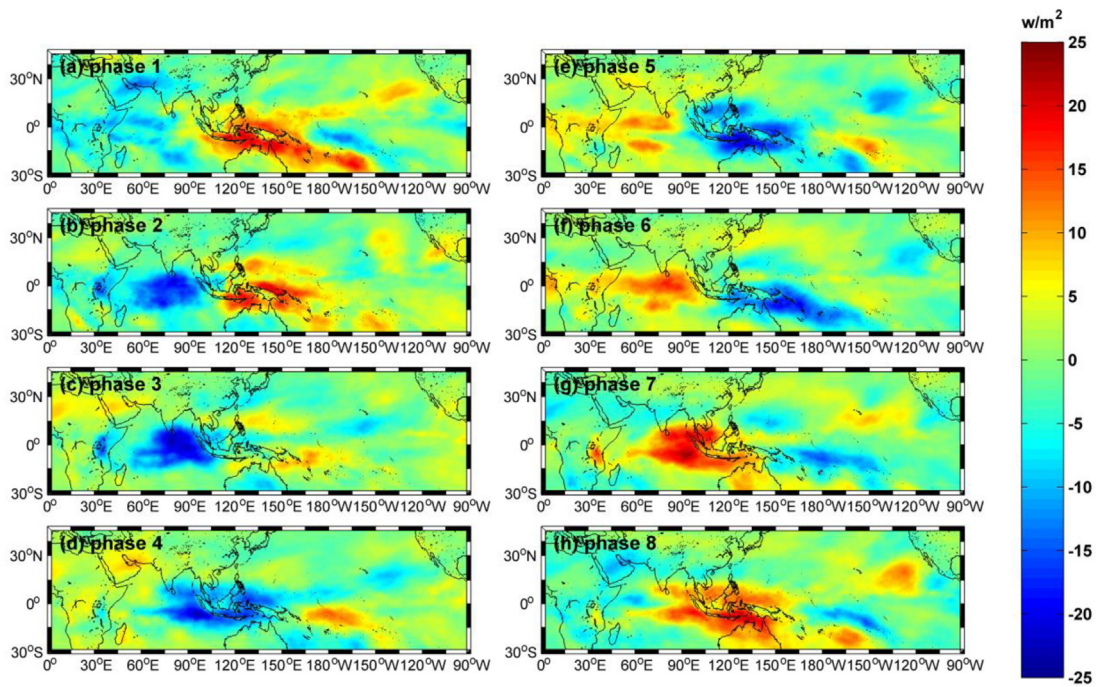


Fig. 10. Composite anomalous (a-h) outgoing long wave radiation (OLR,  $W/m^2$ ) for MJO phases 1-8.

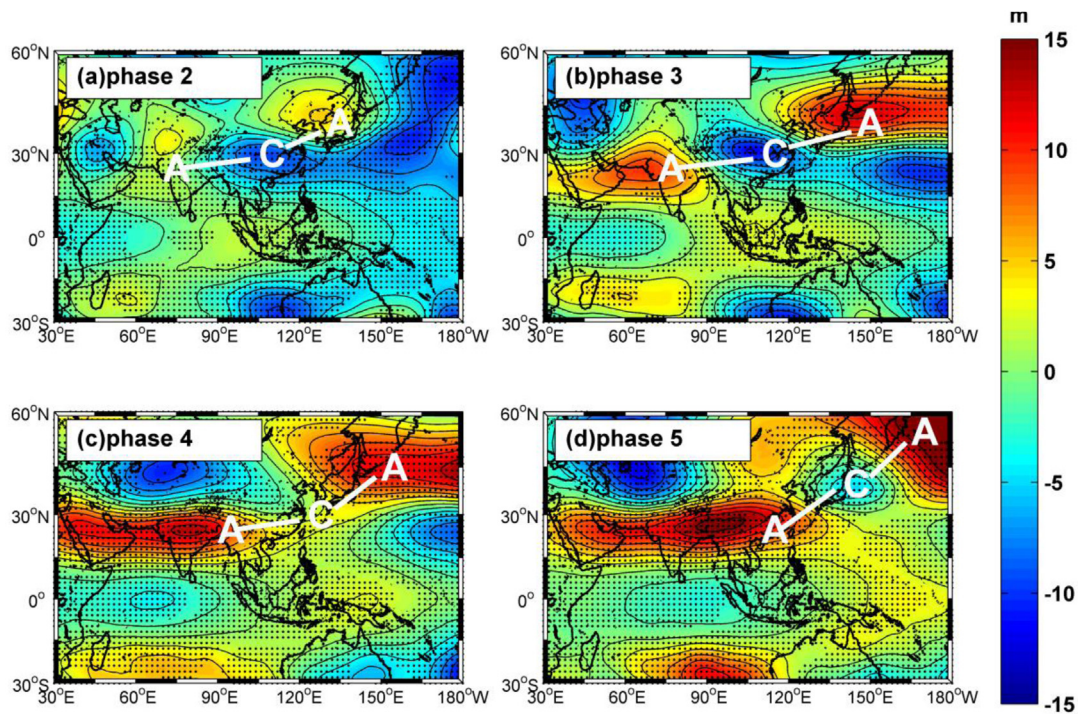
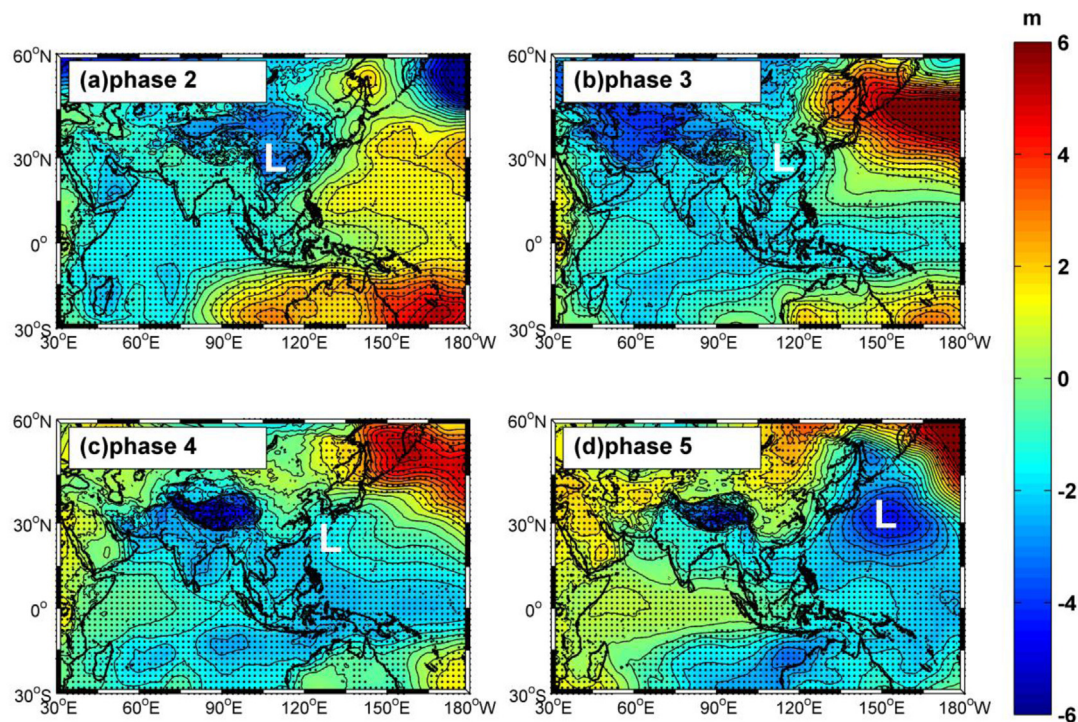


Fig. 11. (a) Composite anomalous 200 hPa geopotential height (color shading with black contours) for MJO phases 2. (b), (c) and (d) are as in (a), but for phases 3, 4, and 5, respectively. The interval of the contours is 2 hPa. Black dot stippling indicates composite anomalies statistically significant at the 90% confidence level via a Student's t test.

at the upper tropospheric level, a cyclonic anomaly at the lower level can be observed in central China in MJO phase 2. Since surface wind is highly correlated with the mean sea level pressure, this cyclonic anomaly results in a strong southwest wind anomaly and hence, a strong northeast volume transport anomaly was observed in the TWS. As the cyclonic anomaly approaches eastward to the near TWS following the eastward shift of the MJO deep convection in the tropics, the southwest wind anomaly weakens in MJO phase 3, resulting in a relatively weak northeast volume transport anomaly in the TWS. After

the cyclonic anomaly pass through the TWS to the east of Taiwan in MJO phase 4, the wind anomaly reversed to northeast, inducing a weak southwest volume transport anomaly in the TWS. During phase 5, the cyclonic anomaly continued to move eastward and reached the east of Japan when TWS was located at its outer edge. This led to a strong northeast wind anomaly and, hence, a strong southwest volume transport anomaly in the TWS.

In summary, the volume transport in the TWS varies as the tropical MJO convection moves from Indian Ocean eastward to the western



**Fig. 12.** (a) Composite anomalous mean sea level pressure (color shading with black contours) for MJO phases 2. (b), (c) and (d) are as in (a), but for phases 3, 4, and 5, respectively. The interval of the contours is 0.5 hPa. Black dot stippling indicates composite anomalies statistically significant at the 90% confidence level via a Student's *t* test.

Pacific Ocean. The physical linkage between the anomalous tropical convection of the MJO and volume transport through the TWS can be explained as follows. The tropical MJO deep convection modulates the upper tropospheric heights through Rossby wave response from the diabatic heating of the MJO convection, generating a wave train pattern that propagates to mid-latitudes. These anomalous upper tropospheric heights adjust the surface pressure field at lower level, resulting in a cyclonic anomaly. When the MJO in the tropics migrates eastward from phase 2 to 5, the upper tropospheric heights anomaly and its corresponding mean sea level pressure anomaly also shift eastward. As the cyclonic anomaly moves from central China in MJO phase 2 to the east of Japan in MJO phase 5, the surface winds respond accordingly to this cyclonic anomaly. This results in a northeast volume transport anomaly during MJO phase 2 and 3 and a southwest volume transport anomaly during MJO phase 4 and 5.

## 5. Conclusions

Based on the simulated results of a three-dimensional operational numerical model, the present study investigates the variability of volume transport in the TWS and its response to tropical MJO convection. The model reproduced the physical field reasonably and showed that the volume transport in the TWS has strong seasonal cycles as well as higher-frequency variations. The intra-seasonal fluctuations dominate the along-strait currents variability, while the secondary and the last signal are seasonal one and inter-annual variability, respectively. The results of SVD analysis and multivariable linear regression model revealed that the along-strait wind stress explains a majority of the volume transport variability in the TWS. The pressure gradient induced by north-to-south sea level slope also explains a part of the variability of the along-strait current, particularly in the two major paths where the northward transport contributes the most. The results of cross-spectra analysis confirmed the significant coherence between the along-strait wind stress and the volume transport through the TWS. The along-strait wind stress generally leads the transport for approximately 0–6 h, suggesting that the flow in the TWS needs a frictional adjustment time

to respond to the changing along-strait wind stress. In comparison, the volume transport has a time lag of roughly 9–22 h to respond to the sea level slope change. This might be attributed to the time taken by coastal-trapped waves to propagate southward through the TWS, modifying the changing cross-strait sea-level gradient and inducing an instantaneous response of volume transport variability.

At intra-seasonal time scales, the movement of the tropical MJO convection from Indian Ocean eastward to the western Pacific Ocean results in varying volume transport in the TWS. Composites of the depth-averaged current anomalies manifest that the TWS displays strong anomalous northeast transport during MJO phase 2 and significantly anomalous southwest transport during MJO phase 5. These oceanic anomalies are shown to be related to atmospheric anomalies, with a distinct physical linkage from the tropical atmosphere to the mid-latitude ocean. The upper tropospheric heights are modified by the tropical MJO deep convection, generating a wave train pattern that propagates to mid-latitudes. These anomalous upper tropospheric heights modulate the surface pressure via quasi-geostrophic adjustment mechanisms and result in a cyclonic anomaly. When the MJO heat source in the tropics migrates eastward from phase 2 to 5, the upper tropospheric heights anomaly and its corresponding mean sea level pressure anomaly also move eastward. The movement of cyclonic anomaly from central China in MJO phase 2 to the east of Japan in MJO phase 5 results in changes in surface winds. Consequently, it results in a northeast volume transport anomaly during MJO phase 2 and 3, and a southwest volume transport anomaly during MJO phase 4 and 5.

The intra-seasonal variability is crucial in a wide array of physical and biological phenomena, including extreme events such as storm surges and cold disasters in the TWS. Liao et al. (2013) explored the occurrence of 2008 cold disaster in the TWS and attributed the abnormal transport of the cold water from the central strait to Penghu Island to the intensified northeasterly winds and the consequent southwest current during its second stage. The potential impacts of MJO on the timing, intensity, and duration of the cold disaster in the TWS require further study. Moreover, the MJO can derive oceanic dynamical variability, including biological activities off the equatorial ocean

(Isoguchi and Kawamura, 2006). The temporal and spatial variability of biological processes in the TWS are modulated by combine forcing of monsoon, complex bottom topography, and the current systems in the TWS. Thus, future research works focusing on the interaction between MJO and the biological processes in the TWS are also needed.

### CRedit authorship contribution statement

**Haowei Sun:** Methodology, Data analysis, Visualization, Writing – original draft. **Zhaoyun Chen:** Data analysis. **Zhonghua Zhao:** Data analysis. **Mengdi Xu:** Data analysis. **Yimin Zhang:** Data analysis. **Xiao-Hai Yan:** Data analysis. **Xueding Li:** Data analysis. **Yuwu Jiang:** Writing – review & editing.

### Declaration of competing interest

The authors declare that they have no known competing financial interests or personal relationships that could have appeared to influence the work reported in this paper.

### Data availability

Data will be made available on request.

### Acknowledgments

This work was supported by the Chinese Ministry of Science and Technology through the National Key Research and Development Program of China (2022YFA1004404). The field work was supported by grant (U22A20579, 41876004) from Natural Science Foundation of China (NSFC). S. Fang, Y. Yu and Z. Xu from Information and Network Center of Xiamen University are acknowledged for the help with the high-performance computing.

### References

- Barrett, B.S., Davies, A.R., Rose, J.I., 2017. Wind-driven response of the upper ocean along the U.S. west coast to tropical MJO convection. *J. Geophys. Res. Oceans* 122, 8196–8207. <http://dx.doi.org/10.1002/2017JC013086>.
- Carlson, T.N., 1991. *Mid-Latitude Weather Systems*. Harper Collins Academic, New York.
- Chang, Y.-L., Miyazawa, Y., Guo, X., 2015. Effect of mesoscale eddies on the Taiwan strait current. *J. Phys. Oceanogr.* 45, 1651–1666. <http://dx.doi.org/10.1175/JPO-D-14-0248.1>.
- Chapman, D.C., 1985. Numerical treatment of cross-shelf open boundaries in a barotropic coastal ocean model. *J. Phys. Oceanogr.* 15, 1060–1075. [http://dx.doi.org/10.1175/1520-0485\(1985\)015%3c1060:NTOCSO%3e2.0.CO;2](http://dx.doi.org/10.1175/1520-0485(1985)015%3c1060:NTOCSO%3e2.0.CO;2).
- Chen, Z., Yan, X.-H., Jiang, Y., 2014. Coastal cape and canyon effects on wind-driven upwelling in northern Taiwan strait. *J. Geophys. Res. Oceans* 119, 4605–4625. <http://dx.doi.org/10.1002/2014JC009831>.
- Chuang, W.-S., 1985. Dynamics of subtidal flow in the Taiwan strait. *J. Oceanogr. Soc. Jpn.* 41, 65–72. <http://dx.doi.org/10.1007/BF02109175>.
- Chuang, W.-S., 1986. A note on the driving mechanisms of current in the Taiwan strait. *J. Oceanogr.* 42, 355–361. <http://dx.doi.org/10.1007/BF02110430>.
- Flather, R.A., 1987. A tidal model of the northeast Pacific. *Atmos. Ocean* 25, 22–45. <http://dx.doi.org/10.1080/07055900.1987.9649262>.
- Fu, Z., Hu, J., Yu, G., 1991. Seawater flux through Taiwan strait. *Chin. J. Oceanol. Limnol.* 9, 232–239. <http://dx.doi.org/10.1007/BF02850748>.
- Gill, A.E., 1980. Some simple solutions for heat-induced tropical circulation. *Q. J. Roy. Meteor. Soc.* 106, 447–462. <http://dx.doi.org/10.1002/qj.49710644905>.
- Guo, J.S., Hu, X.M., Yuan, Y.L., 2005. A diagnostic analysis of variations in volume transport through the Taiwan strait using satellite altimeter data. *Adv. Mar. Sci.* 23, 20–26, (in Chinese with English abstract).
- Hsin, Y.-C., Qiu, B., Chiang, T.-L., Wu, C.-R., 2013. Seasonal to interannual variations in the intensity and central position of the surface Kuroshio east of Taiwan. *J. Geophys. Res. Oceans* 118, 4305–4316. <http://dx.doi.org/10.1002/jgrc.20323>.
- Hsu, H.-H., 1996. Global view of the intraseasonal oscillation during northern winter. *J. Clim.* 9, 2386–2406. [http://dx.doi.org/10.1175/1520-0442\(1996\)009%3c2386:GVOTIO%3e2.0.CO;2](http://dx.doi.org/10.1175/1520-0442(1996)009%3c2386:GVOTIO%3e2.0.CO;2).
- Hu, J., Kawamura, H., Li, C., Hong, H., Jiang, Y., 2010. Review on current and seawater volume transport through the Taiwan strait. *J. Oceanogr.* 66, 591–610. <http://dx.doi.org/10.1007/s10872-010-0049-1>.
- Hung, C., Lin, H.-J., Hsu, H.-H., 2014. Madden–Julian oscillation and the winter rainfall in Taiwan. *J. Clim.* 27, 4521–4530. <http://dx.doi.org/10.1175/JCLI-D-13-00435.1>.
- Isoguchi, O., Kawamura, H., 2006. MJO-related summer cooling and phytoplankton blooms in the south China sea in recent years. *Geophys. Res. Lett.* 33 (L16615), <http://dx.doi.org/10.1029/2006GL027046>.
- Jan, S., Sheu, D.D., Kuo, H.-M., 2006. Water mass and throughflow transport variability in the Taiwan strait. *J. Geophys. Res.* 111 (C12012), <http://dx.doi.org/10.1029/2006JC003656>.
- Jan, S., Wang, J., Chern, C.-S., Chao, S.-Y., 2002. Seasonal variation of the circulation in the Taiwan strait. *J. Mar. Syst.* 35, 249–268. [http://dx.doi.org/10.1016/S0924-7963\(02\)00130-6](http://dx.doi.org/10.1016/S0924-7963(02)00130-6).
- Jones, C., Waliser, D.E., Gautier, C., 1998. The influence of the Madden–Julian oscillation on ocean surface heat fluxes and sea surface temperature. *J. Clim.* 11, 1057–1072. [http://dx.doi.org/10.1175/1520-0442\(1998\)011%3c1057:TlOTMJ%3e2.0.CO;2](http://dx.doi.org/10.1175/1520-0442(1998)011%3c1057:TlOTMJ%3e2.0.CO;2).
- Kashino, Y., Watanabe, H., Herunadi, B., Aoyama, M., Hartoyo, D., 1999. Current variability at the Pacific entrance of the Indonesian throughflow. *J. Geophys. Res.* 104, 11021–11035. <http://dx.doi.org/10.1029/1999JC900033>.
- Ko, D.S., Preller, R.H., Jacobs, G.A., Tang, T.Y., Lin, S.F., 2003. Transport reversals at Taiwan Strait during October and November 1999. *J. Geophys. Res.* 108, 3370. <http://dx.doi.org/10.1029/2003JC001836>.
- Kuang, F.F., Zhang, Y.Q., Zhang, J.P., Jia, C., 2015. Comparison and evaluation of three sea surface wind products in Taiwan strait. *Haiyang Xuebao* 37, 21–30, (in Chinese with English abstract).
- Li, L., Guo, X., Liao, E., Jiang, Y., 2018. Subtidal variability in the Taiwan strait induced by combined forcing of winter monsoon and topography. *Sci. China Earth Sci.* 61, 483–493. <http://dx.doi.org/10.1007/s11430-016-9132-9>.
- Liao, E., Jiang, Y., Li, L., Hong, H., Yan, X., 2013. The cause of the 2008 cold disaster in the Taiwan strait. *Ocean Model.* 62, 1–10. <http://dx.doi.org/10.1016/j.ocemod.2012.11.004>.
- Liao, E., Oey, L.Y., Yan, X.-H., Li, L., Jiang, Y., 2018. The deflection of the China coastal current over the Taiwan bank in winter. *J. Phys. Oceanogr.* 48, 1433–1450. <http://dx.doi.org/10.1175/JPO-D-17-0037.1>.
- Lin, S.F., Tang, T.Y., Jan, S., Chen, C.-J., 2005. Taiwan strait current in winter. *Cont. Shelf Res.* 25, 1023–1042. <http://dx.doi.org/10.1016/j.csr.2004.12.008>.
- Lin, X., Yan, X.-H., Jiang, Y., Zhang, Z., 2016. Performance assessment for an operational ocean model of the Taiwan strait. *Ocean Model.* 102, 27–44. <http://dx.doi.org/10.1016/j.ocemod.2016.04.006>.
- Liu, W.T., Katsaros, K.B., Businger, J.A., 1979. Bulk parameterization of air-sea exchanges of heat and water vapor including the molecular constraints at the interface. *J. Atmos. Sci.* 36, 1722–1735. [http://dx.doi.org/10.1175/1520-0469\(1979\)036%3c1722:BPOASE%3e2.0.CO;2](http://dx.doi.org/10.1175/1520-0469(1979)036%3c1722:BPOASE%3e2.0.CO;2).
- Madden, R.A., Julian, P.R., 1971. Detection of a 40–50 day oscillation in the zonal wind in the tropical pacific. *J. Atmos. Sci.* 28, 702–708. [http://dx.doi.org/10.1175/1520-0469\(1971\)028%3c0702:DOADOI%3e2.0.CO;2](http://dx.doi.org/10.1175/1520-0469(1971)028%3c0702:DOADOI%3e2.0.CO;2).
- Madden, R.A., Julian, P.R., 1972. Description of global-scale circulation cells in the tropics with a 40–50 day period. *J. Atmos. Sci.* 29, 1109–1123. [http://dx.doi.org/10.1175/1520-0469\(1972\)029%3c1109:DOGSCC%3e2.0.CO;2](http://dx.doi.org/10.1175/1520-0469(1972)029%3c1109:DOGSCC%3e2.0.CO;2).
- Matsuno, T., 1966. Quasi-geostrophic motions in the equatorial area. *J. Meteorol. Soc. Jpn.* 44, 25–43. [http://dx.doi.org/10.2151/jmsj1965.44.1\\_25](http://dx.doi.org/10.2151/jmsj1965.44.1_25).
- Mellor, G.L., Yamada, T., 1982. Development of a turbulence closure model for geophysical fluid problems. *Rev. Geophys.* 20 (851), <http://dx.doi.org/10.1029/RG020i004p00851>.
- Shchepetkin, A.F., McWilliams, J.C., 2003. A method for computing horizontal pressure-gradient force in an oceanic model with a nonaligned vertical coordinate. *J. Geophys. Res.* 108, 3090. <http://dx.doi.org/10.1029/2001JC001047>.
- Shchepetkin, A.F., McWilliams, J.C., 2005. The regional oceanic modeling system (ROMS): A split- $\epsilon$  explicit, free-surface, topography-following-coordinate oceanic model. *Ocean Model.* 9, 347–404. <http://dx.doi.org/10.1016/j.ocemod.2004.08.002>.
- Shen, J., Qiu, Y., Guo, X., Pan, A., Zhou, X., 2017. The spatio-temporal variation of wintertime subtidal currents in the western Taiwan strait. *Acta Oceanol. Sin.* 36, 4–13. <http://dx.doi.org/10.1007/s13131-017-1120-1>.
- Shinoda, T., Jensen, T.G., Flatau, M., Chen, S., 2013. Surface wind and upper-ocean variability associated with the Madden–Julian oscillation simulated by the coupled ocean–atmosphere mesoscale prediction system (COAMPS). *Mon. Weather Rev.* 141, 2290–2307. <http://dx.doi.org/10.1175/MWR-D-12-00273.1>.
- Waliser, D.E., 2003. Indo-Pacific ocean response to atmospheric intraseasonal variability: 1. Austral summer and the Madden-Julian oscillation. *J. Geophys. Res.* 108, 3160. <http://dx.doi.org/10.1029/2002JC001620>.
- Wang, J., Hong, H., Jiang, Y., 2016. A coupled physical–biological modeling study of the offshore phytoplankton bloom in the Taiwan strait in winter. *J. Sea Res.* 107, 12–24. <http://dx.doi.org/10.1016/j.seares.2015.11.004>.
- Wang, Y.H., Jan, S., Wang, D.P., 2003. Transports and tidal current estimates in the Taiwan strait from shipboard ADCP observations (1999–2001). *Estuar. Coast. Shelf Sci.* 57, 193–199. [http://dx.doi.org/10.1016/S0272-7714\(02\)00344-X](http://dx.doi.org/10.1016/S0272-7714(02)00344-X).

- Wang, G., Ling, Z., Wu, R., Chen, C., 2013. Impacts of the Madden–Julian oscillation on the summer south China sea ocean circulation and temperature. *J. Clim.* 26, 8084–8096. <http://dx.doi.org/10.1175/JCLI-D-12-00796.1>.
- Wheeler, M.C., Hendon, H.H., 2004. An all-season real-time multivariate MJO index: Development of an index for monitoring and prediction. *Mon. Wea. Rev.* 132, 1917–1932. [http://dx.doi.org/10.1175/1520-0493\(2004\)132%3c1917:AARMMI%3e2.0.CO;2](http://dx.doi.org/10.1175/1520-0493(2004)132%3c1917:AARMMI%3e2.0.CO;2).
- Wu, H., Deng, B., Yuan, R., Hu, J., Gu, J., Shen, F., Zhu, J., Zhang, J., 2013. Detiding measurement on transport of the Changjiang-derived buoyant coastal current. *J. Phys. Oceanogr.* 43, 2388–2399. <http://dx.doi.org/10.1175/JPO-D-12-0158.1>.
- Wu, C.-R., Hsin, Y.-C., 2005. Volume transport through the Taiwan strait: A numerical study. *Terr. Atmos. Ocean. Sci.* 16 (377), [http://dx.doi.org/10.3319/TAO.2005.16.2.377\(Oc\)](http://dx.doi.org/10.3319/TAO.2005.16.2.377(Oc)).
- Wyrtki, K., 1961. *Physical Oceanography of the Southeast Asian Waters*, Vol. 2. University of California, Scripps Institution of Oceanography.
- Yang, J., 2007. An oceanic current against the wind: How does Taiwan island steer warm water into the east China sea? *J. Phys. Oceanogr.* 37, 2563–2569. <http://dx.doi.org/10.1175/JPO3134.1>.
- Zhang, W.-Z., Chai, F., Hong, H.-S., Xue, H., 2014. Volume transport through the Taiwan strait and the effect of synoptic events. *Cont. Shelf Res.* 88, 117–125. <http://dx.doi.org/10.1016/j.csr.2014.07.010>.
- Zhang, W.-Z., Hong, H.-S., Shang, S.-P., Yan, X.-H., Chai, F., 2009. Strong southward transport events due to typhoons in the Taiwan strait. *J. Geophys. Res.* 114 (C11013), <http://dx.doi.org/10.1029/2009JC005372>.
- Zhang, W.-Z., Hong, H.-S., Yan, X.-H., 2013. Typhoons enhancing northward transport through the Taiwan strait. *Cont. Shelf Res.* 56, 13–25. <http://dx.doi.org/10.1016/j.csr.2013.01.019>.
- Zhao, Z., Lin, J., Fu, J., Jiang, Y., 2020. Cold water anomalies in the middle layer of the northern Taiwan strait in spring—a numerical approach. *Ocean Dyn.* 70, 1571–1585. <http://dx.doi.org/10.1007/s10236-020-01412-1>.